Tribological and Micromechanical Properties of the Nanostructured Carbonitride/Nitride Coatings of Transition Metals Alloyed by Hf and Nb

Armands Leitans [1,*], Ernests Jansons [1], Janis Lungevics [1], Karlis Kundzins [1,2], Irina Boiko [1], Uldis Kanders [1], Vladimirs Kovalenko [3] and Oskars Linins [1]

[1] Institute of Mechanics and Mechanical Engineering, Faculty of Mechanical Engineering, Transport and Aeronautics, Riga Technical University, Kipsala Street 6b, LV-1048 Riga, Latvia

[2] Institute of Solid State Physics, University of Latvia, Kengaraga Street 8, LV-1063 Riga, Latvia

[3] Research Division of the Naco Technologies Ltd., Ganibu dambis 24A-52, LV-1005 Riga, Latvia

[*] Correspondence: armands.leitans@rtu.lv

Abstract: In this article, the fabrication, characterization, tribological performance, and micromechanical properties of nanostructured smart coatings (NSC) based on the multilayered alternating carbonitride/nitride bilayer {Ti*Me*-CN/TiAlSi-N}*n* system are discussed. The symbol "*Me*" denotes refractory metals Hf or Nb, and the index "*n*" shows the number of superlattice periods. The NSC samples were deposited onto bearing steel (100Cr6) substrates using a reactive high-power physical vapor deposition (PVD) technique that can be scaled up for industrial use. The deposited multilayered NSC contained crystalline nanometer-scale Ti*Me*-CN/TiAlSi-N nanoparticles strengthened by Hf or Nb additives, which increased surface microhardness up to 3000 HV. The measured steady-state friction coefficient (CoF) was within the 0.2–0.4 range, and a specific wear rate lower than 2×10^{-6} mm^3/Nm was observed in the dry friction regime. The impact of NSC substrate hardness and NSC coating thickness on microhardness measurement values was investigated. A thicker coating provided a higher integrated (coating + substrate) microhardness value at a lower indentation test force (<0.3 N). As the indentation test force increased, the obtained microhardness values decreased faster for the coatings deposited on a softer substrate. The surface roughness impact on wear properties for specific NSC coatings was observed.

Keywords: carbonitride/nitride coatings; superlattice; micro-indentation; microhardness; tribological performance; wear; friction coefficient; surface texture

1. Introduction

Hard (<40 GPa) and super-hard (>40 GPa) coatings based on transition metal nitrides and carbonitrides are of great interest due to their high hardness, chemical inertness, and excellent wear resistance [1–3]. Such nitride-type nanocomposite coatings as TiN, TiCN, TiAlN, and TiAlSiN [4], which are developed for steel-cutting tools to increase their lifetime, are of great interest. Furthermore, incorporating small amounts of Al and Si constituents into the nanocomposite structure significantly improves tribological and anti-corrosive properties such as hardness, wear resistance, thermal stability, and denitrification temperature [5]. It is known that TiAlSiN nanocomposite films can be deposited by several different physical vapor deposition (PVD) techniques, resulting in different coating performances. Often, the brittleness of hard ceramic TiAlSiN-type coatings, such as the amorphous carbon (a-C) and diamond-like coatings (DLC) [6,7], severely limits their practical application. Additionally, the pure carbon films including DLC coatings exhibit relatively low adhesion to the substrate and insufficient toughness for machine components. Therefore, new modified PVD techniques are needed to ensure that deposited coatings can perform as expected. The toughness of hard ceramic coatings such as TiAlSiN depends mainly on their micro-

and nano-structure, which might not be dense enough due to micropores and nanovoids causing cracks and delamination phenomena [8,9].

Nanostructured multilayer coatings based on alternating nitride/nitride and/or carbonitride/nitride bilayer structures of transition metals deposited by reactive magnetron sputtering (N_2/Ar gas mixture) have been of great interest for a long time. Besides, using a multilayered coating architecture allows the design of coatings with enhanced tribological performance and micromechanical properties that surpass those inherent in corresponding monolayered coatings [9–11].

Despite the many research works and developments in the field of hard nano-coatings mentioned above, to combine ultra-low friction-wear properties all in one coating is still a great challenge. Recently, a novel approach to further improve the tribological and micromechanical properties of the alternating multilayered coatings by the incorporation of new nanocrystalline, nanocomposite, or even amorphous constituent components by an advanced PVD technique, denoted here as high-power ion-plasma magnetron sputtering (HiPIPMS), was proposed by the authors [12,13]. Therefore, the research strategy was based on modified non-stoichiometric carbonitride/nitride bilayer Ti*Me*-CN/TiAlSi-N, where *Me* = Hf or Nb, for achieving a novel solution to sufficiently reduce or even eliminate the well-known disadvantages of the pure hard carbon- or nitride-based films, i.e., inherent compressive macro-stresses, not-good-enough adhesion to steel workpieces, and reduced thermal stability. The aim of this paper is to examine the tribological performance and micromechanical properties of the nanostructured carbonitride/nitride coatings of transition metals alloyed by Hf and Nb produced using the advanced PVD technique (HiPIPMS). Additionally, the influence of the hardness of the substrate and the surface texture on the tribological properties is investigated. As expected, the using the novel approach for the fabrication of nanostructured smart coatings (NSC) based on the multilayered alternating carbonitride/nitride bilayer {Ti*Ci*-CN/TiAlSi-N}n system (the symbol "*Me*" denotes refractory metals Hf or Nb, and the index "*n*" shows the number of superlattice periods) provides a promising set of tribological properties of NSC samples which can be scaled up for industrial use.

2. Materials and Methods

2.1. Preparation of the NSC Samples

The advanced PVD technique was used to deposit thin-film coatings onto the 100Cr6-bearing steel substrate. The HiPIPMS was implemented on the thin-film modular deposition system (TF-MDS) [14]. The term HiPIPMS is used here in the sense of a specific advanced PVD technique allowing to exceed a discharge power density higher than 60 W/cm^2 within the erosion zone of the magnetron sputtering target (MST). The HiPIPMS device, MSD, was equipped with MST without a backing plate, in contrast to the conventional DC PVD method using MST with a backing plate in combination with insufficiently intense bubbling water cooling of a comparably low flow rate underneath the backing plate. There is no special secret concerning how to exceed the 60 W/cm^2 threshold for discharge power of the magnetron sputtering devices (MSD). Contrasted with the conventional PVD method, the HiPIPMS deposition systems use magnetically intensive MSDs (B-field about 600–900 mT) equipped with the MSTs without backing plates, in combination with very efficient bubble-free water cooling of a high flow rate directly underneath the MSTs. The cooling water pressure was maintained at about 5–7 bars.

It is known that the current state of the conventional DC PVD method, in contrast to the HiPIPMS technique, does not allow for expanding the scope of its application for the manufacture of many types of products used in various fields of high-tech applications. These limitations are due to: (1) relatively low deposition rates of the material (up to 5 μm/h), (2) an insufficiently high degree of ionization of sputtered particles and a decrease in adhesion with a coating thickness greater than 5 μm, (3) the complexity of the joint deposition of materials with significantly different sputtering yields, and (4) high requirements for the cleanliness of the substrate surface (roughness (Rq—root mean square deviation of

the profile) should not be more than 0.2–0.3 microns). These limitations of the conventional PVD methods exist because, in the known setups, it is impossible to provide a discharge power density higher than 40 W/cm^2 of the MST surface area within its maximum erosion zone. After all, 40 W/cm^2 is a substantial threshold value for the equal sputtering rate of mosaic-type MST of different materials. At such a relatively low MSD discharge power of less than 40 W/cm^2, the sputtering rate of each component of the mosaic-type MST designed with different materials is primarily determined by their sputtering yields. Therefore, the atomic ratio of the sputtered particles of the mosaic-type MST components in the vapor phase is practically uncontrollable, raising significant technological difficulties for using the conventional PVD method to deposit coatings of complex chemical composition. This problem significantly limits the possibilities of using this technique. In addition, mosaic-type MST components made of transition metals, and moreover of the refractory metals for the manufacture of coatings, are challenging to alloy or press into a target of the required chemical composition and geometric shape (plates, bushings, or pipes). Thus, it is necessary to carry out separate sputtering of the components, such as mosaic-type MST. For example, a coating of carbon and transition metal was obtained, and separate sputtering of graphite and chromium targets was carried out. In this case, it is necessary in each particular case to solve the complex problems of calculating the geometry of the targets, selecting the sputtering rates for each of the components and the technological parameters of the sputtering process, ensuring homogeneous mixing of the atomic vapor flows of the sputtered components, and uniform deposition of the components on the substrate in the form of a coating of a given composition. The disadvantage of separate sputtering of targets is the difficulty of obtaining coatings consisting of three or more components, especially in cases where the coefficients of sputtering of the materials of these targets vary largely and strongly depend on process parameters, for example, operating sputter gas pressure, temperature, magnetic permeability, current, and discharge voltage.

The TF-MDS used in this study had four cross-configured workstations equipped with magnetron sputtering devices (MSD). The cross-configuration of the workstations on the circumference inside the vacuum chamber allows numerous specific combinations of monolithic and mosaic-type magnetron sputtering targets (MST) mounted on MDS, depending on the requested chemical composition of the NSC. MSDs were operated in the effective cross-field unbalanced magnetron sputtering ion-plasma mode, which provided a highly ionized plasma environment in the whole MST and substrate-holder section. As a result, immersed sputtering plasma mode was realized on the substrate surface. The plasma environment enhanced the chemical reactivity of the sputtered particles that condensed on the substrate and activated carbonitride/nitride film growth. Sputter cleaning of the substrates was performed prior to film deposition by a collimated linear ion beam device, which was also used for film-growing activation and re-sputtering weakly accommodated particles during the film deposition process.

The most significant technological parameters of the HiPIPMS-PVD process regarding the MST sputtering and NSC growth were the following: (i) Base pressure in the vacuum chamber before the PVD process, p_b = 0.131 mPa, (ii) total operating gas pressure of the sputter gas mixture (Ar/N$_2$), p_{sg} = 0.36 Pa, and (iii) partial gas flow rate, q_{gN2} = 12.4 L/h. (iv) Prior to film deposition, substrate heating and in situ sputter cleaning were performed using collimated linear ion beam etching at 1800 V × 140 mA. (v) The distance between MSD and substrate L = 85 mm, (vi) the substrate temperature during the PVD deposition process was kept at 340 °C, and (vii) the electrical discharge power regime of MSDs was varied within (630–690) V × (7.4–9.8) A depending on the sputter gas mixture ratio, the design and configuration of the MSTs, and their total working surface. Besides, the DC discharge power density of the operating MSDs exceeded the 60 W/cm^2 threshold value needed for equal-rate sputtering conditions of the mosaic-type sputtering targets [15]. (viii) The NSC film sample deposition rate at 2D rotation was kept at 180 nm/min, and (ix) negative bias voltage during the deposition process was maintained at 90 V, causing the bias current of about 350–500 mA depending on the sputter discharge power.

The Calo tester (CSM Instruments, Peseux, Switzerland) and digital microscope KH-7700 (Hirox, Tokyo, Japan) were used to measure the thickness of the deposited coatings.

2.2. Tribological Tests of the NSC Samples

The NSC sample tribology tests were conducted with a ball-on-disc-type tribometer, TRB^3 (CSM Instruments SA, Peuseux, Switzerland), under dry friction conditions, according to the standard ISO 18535:2016 (Diamond-like carbon films—determination of friction and wear characteristics of diamond-like carbon films by ball-on-disc method) recommendations. The most commonly used 100Cr6 (EN 683-17:2014, Heat-treated steels, alloy steels, and free-cutting steels—Part 17: Ball- and roller-bearing steels) steel ball with a 6 mm diameter was used as the static friction partner in tribology experiments to ensure the possibility of comparing these research results with other studies that use the same material [16–19]. The following experiment settings were used: 100 m sliding distance, 3 N applied load, 3 mm wear track radius, and 0.05 m/s linear sliding speed. All tests were conducted at a 22 ± 1 °C temperature. After the tribology test, the sample wear track profiles were measured at four evenly distributed locations with a profilometer Surftest SJ-500 (Mitutoyo, Kawasaki, Japan). The worn-out cross-sectional area of the wear track profiles was calculated using the software MCube Map Ultimate 8.0 (Mitutoyo, Kawasaki, Japan). The specific wear rate of the NSC was then calculated using an average value of all four worn-out cross-sectional areas. The wear of the static friction partner was measured with a digital microscope KH-7700 (Hirox, Tokyo, Japan).

2.3. Micro-Indentation Hardness Tests

Micro-indentation hardness tests provided information about the integrated coating hardness, including the hardness of both the coating and the substrate. NSC sample micro-indentation hardness tests were performed using a micro-Vickers hardness testing machine HM-210D (Mitutoyo, Kawasaki, Japan), which works according to ISO 6507-2:2018 (Metallic materials—Vickers hardness test—Part 2: Verification and calibration of testing machines). The motor-controlled XY sample stage, in combination with AVPAK 3.0 software, allowed the creation of a test matrix where indentations in XY directions were spaced 300 μm apart. Twenty different indentation loads between the range of 0.10 to 6.88 N were used, and ten indentations were performed for each test load to obtain better measurement statistics. The test matrix sketch is shown in Figure 1. The test load step of 0.098 N was used in the load range from 0.1 N to 0.98 N, and the 0.49 N load step was used in the load range from 0.98 N to 5.88 N. All indentations were measured with a 100× g magnification lens to ensure the highest resolution.

2.4. NSC Sample Adhesion Testing

The NSC sample adhesion was checked with the Rockwell (scale C) test method according to DIN 4856: 2018-02 (Carbon-based films and other hard coatings—Rockwell penetration test to evaluate the adhesion) guidelines. A conical diamond indenter (cone angle 120°, tip radius 0.2 mm) was pierced in the NSC surface with a 150 N force using the Rockwell hardness tester HR-200 (Mitutoyo, Kawasaki, Japan). The coating damage around the indentation imprint was then observed with a digital microscope KH-7700 (Hirox, Tokyo, Japan). The coating damage was categorized into one of six adhesion classes, HF1–HF6, defined in the standard. Adhesion classes are based on crack density and delamination intensity after the Rockwell hardness test.
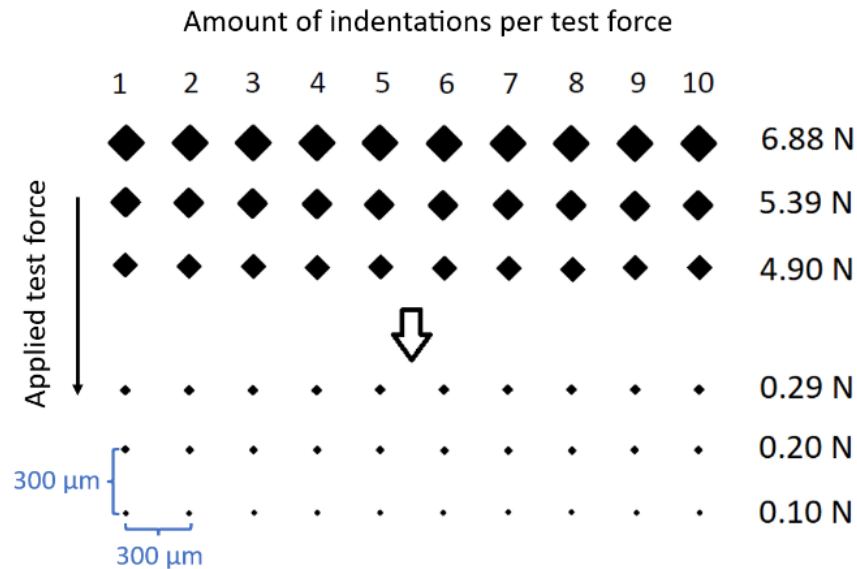
Figure 1. Micro-indentation hardness test matrix. Ten measurements with twenty different test forces were performed to analyze the coating's microhardness. Indentations were spaced 300 micrometers apart in both X and Y directions. Ten indentations were performed for each test force.

2.5. Surface Roughness Measurements

The 2D roughness measurements were performed using a Surftest SJ-500 (Mitutoyo, Kawasaki, Japan) roughness tester. Roughness measurement conditions were set according to ISO 21920-3:2021 (Geometrical product specifications (GPS)—Surface texture: Profile—Part 2: Terms, definitions, and surface texture parameters). Three profiles were measured from the sample center towards the outside, and average Ra (arithmetical mean deviation of the profile), Rq (root mean square deviation of the profile), Rz (maximum height of the profile), and RSm (mean profile spacing) values were calculated for each sample.

2.6. Electron Microscopy Examinations of the NSC Samples

The morphology of the NSC sample structures was investigated with a scanning electron microscope (SEM), Lyra3 (Tescan, Brno, Czech Republic), equipped with an energy-dispersive X-ray spectrometer (EDS), AZtec (Oxford Instruments, Abingdon, United Kingdom). SEM and EDS measurements were performed using a beam-accelerating voltage of up to 30 kV and a beam current of 500 pA.

3. Results and Discussion

3.1. NSC Samples

During the reactive PVD process, the coating's basic carbonitride/nitride bilayer structure {Ti*Me*-CN/TiAlSi-N} was modified by refractory metals *Me* = Hf and Nb as alloying additives to strengthen the basic carbonitride/nitride bilayer structure of the NSC. The corresponding modified bilayer structures here are denoted as {TiHf-CN/TiAlSi-N} and {TiNb-CN/TiAlSi-N}, respectively. Special mosaic-type MSTs were fabricated to implement the bilayer structures, containing relevant Hf- and Nb-inserts within the round planar MST's annular erosion zone, respectively. Besides, the cross-field configuration of the corresponding mosaic-type MSTs, on the one hand, and the rotating carousel of the substrate holder, on the other hand, allowed the deposition of a superlattice-type nanostructured coating [20].

Thus, the tribology and solid-state mechanics of the superlattice-type NSC samples were investigated, and measurement results are discussed below. The Hf-additive was used for samples NSC-1, NSC-2, and NSC-3. However, the Nb-additive was used for samples NSC-4, NSC-5, and NSC-6 (see Table 1) to monitor the NSC's tribological performance and mechanical properties depending on the peculiarities caused by the additives' interaction with the basic carbonitride/nitride bilayer structure of the NSC samples.

The six NSC samples included in Table 1 were selected from a large number of carbonitride/nitride film samples obtained by the high-power ion-plasma magnetron sputtering (HiPIPMS) technique for a comparably long period. That is why all the selected superlattice samples are not, for example, equally thick or do not have the same periodicity, etc. For this research, alternating multilayered composite coatings of the transition metals were selected. These alternating structures were based on the carbonitride/nitride bilayer alloyed by refractory metals Hf or Nb. The NSC samples had different thicknesses because of the different sputtering rates due to specific MST combinations for each NSC sample and the duration of the deposition processes, which were not especially harmonized. The coating thickness does not play a significant role during tribological tests until the total coating wear does not exceed the NSC thickness. The characteristic thickness of 1–6 microns is good enough for the coating's comprehensive mechanical and tribological investigation. Therefore, the mechanical and tribological properties of the NSC samples are undoubtedly comparable despite the different thicknesses of the coatings.

Table 1. A brief characterization of the superlattice periodic structure of the NSC samples: the total coating thickness, periodicity, and thickness of the carbonitride/nitride bilayers, t_1/t_2, are shown.

Sample Label	Carbonitride/Nitride Bilayer	Coating Thickness (nm)	Number of Periods	PVD process Duration (min)	t_1(-CN), Ti*Me*-CN, (nm)	t_2(-N), TiAlSi-N, (nm)	Period $\Lambda = t_1 + t_2$, (nm)
NSC-1	{TiHf-CN/TiAlSi-N}	~4800	720	120	4.4	2.2	6.6
NSC-2	{TiHf-CN/TiAlSi-N}	~6300	900	150	4.6	2.4	7.0
NSC-3	{TiHf-CN/TiAlSi-N}	~6200	900	150	4.6	2.3	6.9
NSC-4	{TiNb-CN/TiAlSi-N}	~4200	1080	180	2.6	1.3	3.9
NSC-5	{TiNb-CN/TiAlSi-N}	~3400	720	120	3.0	1.7	4.7
NSC-6	{TiNb-CN/TiAlSi-N}	~2300	540	90	2.7	1.5	4.2

The SEM study of the NSC samples' surface morphologies revealed that the coatings doped by Hf had a nodule-like microstructure, and the coatings doped by Nb had a cellular microstructure (Figure 2). Embedded nodules, with sizes ranging from several tens to hundreds of nanometers, separated by notches and nanovoids along grain boundaries, pose a relatively dense packing of sputtered atoms. The micrographs revealed that the NSC samples prepared at the substrate temperature of about 400–450 °C exhibited a pronounced columnar microstructure with inherent notches and nanovoids between densely packed columns that are a typical morphology for the transitional Zone-T between Zone-1 and Zone-2 of the Thornton model regarding film growth [21]. All samples doped by Hf exhibited a granular microstructure, showing strongly elongated grains with an aspect ratio of about 1:3 (Figure 2, top panel), and all the samples doped by Nb exhibited cauliflower-like microstructures, having polygonal domains from a hundred to hundreds of nanometers in size (Figure 2, bottom panel). Due to the coarse cauliflower-like columnar microstructure, the second sample set doped with Nb coatings had deeper notches and nanovoids within the bulk coating. As a result, adsorption of atmospheric moisture and oxygen is very likely to occur in the gaps between the microstructural columns deeper within a bulk beneath the coating's surface.
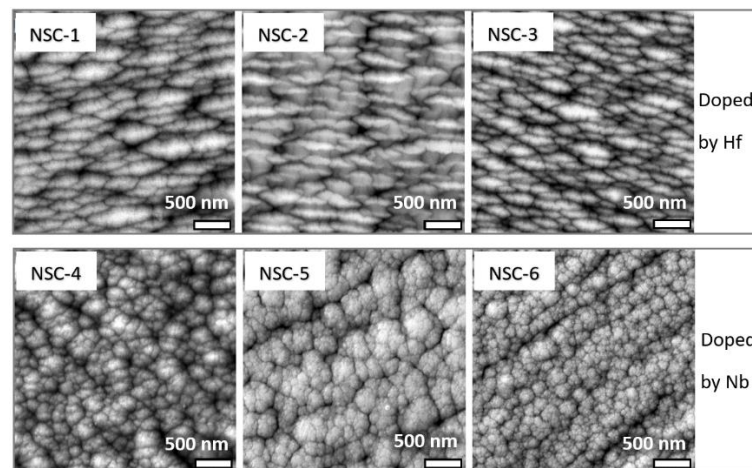
Figure 2. SEM surface micrographs (plan view) of the NSC samples doped by Hf (top panel with NSC-1, NSC-2, and NSC-3) and doped by Nb (bottom panel with NSC-4, NSC-5, and NSC-6). Images show identical morphology for all three samples having the same doping element.

This circumstance caused subsequent oxide formation and denitrification of the coating, thereby facilitating the breakdown of intercolumnar bonds. These oxidation processes in the bulk of the coating were less extensive for samples doped with Hf due to its denser microstructure, resulting in a higher tribological performance than samples doped with Nb.

SEM-EDS analysis was applied to determine the elemental composition of individual NSC samples to map out the lateral distribution of elements from the imaged area. SEM-EDS elemental microanalysis of the NSC samples is shown in Figure 3.
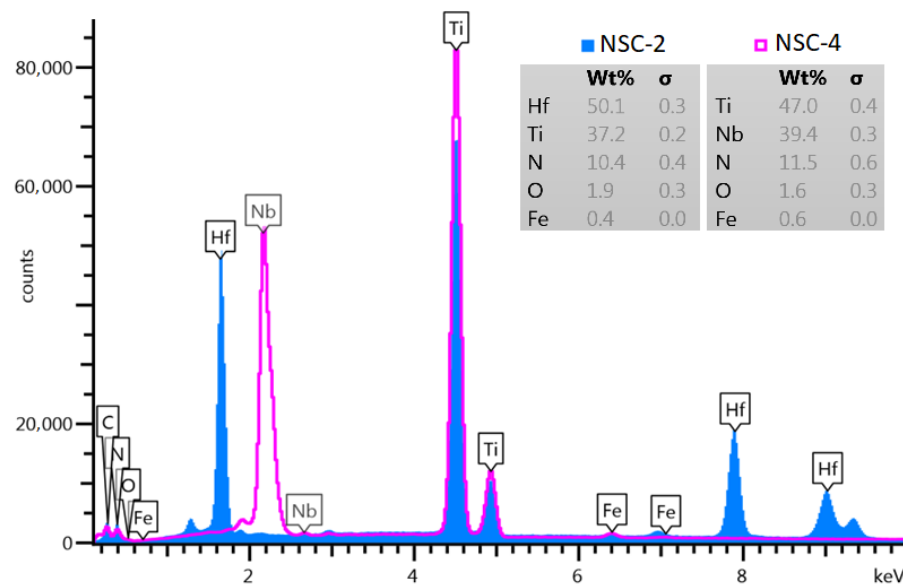
Figure 3. SEM-EDS elemental microanalysis of the NSC samples doped by the atomic elements of Hf (NSC-2) and Nb (NSC-4). The elemental composition was identical for samples doped with the same elements ((NSC-1, NSC-2, and NSC-3) and (NSC-4, NSC-5, and NSC-6)).

3.2. Tribological and Micromechanical Properties

NSC samples doped with Nb and Hf were deposited on bearing steel 100Cr6 substrates with different hardness values. For samples NSC-2, NSC-3, and NSC-4, the substrate hardness was below 20 HRC, but for samples NSC-1, NSC-5, and NSC-6, the substrate hardness was in the range of 55–60 HRC. Hardness values lower than 20 HRC indicated that the substrate annealing had taken place for these samples during the NSC deposition

process, operating magnetrons at a discharge power of about 2 kW or higher. During the PVD deposition process, the substrate temperature was kept at 340 °C as a default, which is significantly lower than the critical temperature of around ~500 °C when tempering of the bearing steel can begin. It was assumed that the thermal stability of the three (NSC-2, NSC-3, and NSC-4) samples was insufficient to withstand the highly intensive magnetron ion–plasma thermal interaction with these substrates. The thermal shock induced by the magnetron discharge power has not affected the film growth process because the Hf and Nb patterns remained unchanged with respect to the thermal annealing of the substrates. Substrate annealing during the PVD process made it possible to see if the substrate hardness affected the coatings' tribological and micromechanical properties. A substrate with a 58 ± 2 HRC hardness was used as a reference to compare the tribological and micromechanical properties of the coatings.

3.2.1. Surface Roughness

The 2D roughness parameters—Ra, Rq, Rz (amplitude parameters influencing friction and wear [22]), and RSm (spacing parameter used for wear calculations [23])—were used to characterize the NSC sample surface texture (see Table 2).

Table 2. NSC sample 2D roughness values.

2D Roughness Parameter (μm)	NSC-1	NSC-2	NSC-3	NSC-4	NSC-5	NSC-6
Ra	0.07 ± 0.01	0.11 ± 0.01	0.33 ± 0.03	0.07 ± 0.01	0.05 ± 0.01	0.06 ± 0.01
Rq	0.12 ± 0.02	0.23 ± 0.02	0.47 ± 0.03	0.12 ± 0.01	0.07 ± 0.01	0.07 ± 0.01
Rz	0.89 ± 0.22	1.65 ± 0.43	2.61 ± 0.61	0.81 ± 0.21	0.42 ± 0.16	0.38 ± 0.14
RSm	11.9 ± 0.98	21.5 ± 1.65	20.9 ± 1.21	13.8 ± 1.17	11.3 ± 1.15	14.8 ± 1.13

Samples NSC-1, NSC-4, NSC-5, and NSC-6 had the lowest surface roughness (Ra below 0.07 μm), and sample NSC-3 had the highest surface roughness (Ra ~0.33 μm). The standard deviation of Ra for all samples did not exceed 0.03 μm, Rz 0.61 μm, and RSm 1.65 mm, respectively. It was noticed that the NSC coating copied the initial substrate texture, i.e., if the substrate had some scratches, they were also visible after NSC deposition.

3.2.2. Friction Coefficient and Wear Rate

The steady-state friction coefficient (CoF) was primarily used to compare coating friction properties (see Table 3). The steady-state CoF was calculated from the friction coefficient curve section where the CoF had a stable value for at least a twenty-meter range. The lowest steady-state CoF values were observed for all samples with the Hf dopant (NSC-1, NSC-2, and NSC-3), ranging from 0.25 to 0.28. The steady-state CoF value for the Nb-doped samples ranged from 0.30 to 0.46. All NSC coatings significantly reduced the steady-state CoF over the 100Cr6 substrate material on which they were deposited, reaching up to a 3× CoF reduction for Hf-doped samples and up to a 2.5× reduction for Nb-doped samples.

To compare NSC sample wear resistance, a specific wear rate was used. It was calculated using the cross-sectional profile area measurements of the worn-out tribotrack obtained in four evenly distributed locations (examples of cross-sectional profile area measurements for each NSC are shown in Appendix A Figure A1). The static friction pair (100Cr6 steel ball) wear rate was also included (see Appendix B Figure A2). Sample NSC-1 had the lowest specific wear rate, while sample NSC-3 had the highest. All NSC samples showed noticeable improvements over the uncoated 100Cr6 substrate that was used as a reference.

Table 3. Overview of the friction and wear properties.

Sample Label	Steady-State CoF	Max CoF	Min CoF	Initial CoF	Specific Wear Rate, (mm^3/Nm)	Static Friction Partner Wear Rate (mm^3/Nm)
NSC-1	0.25 ± 0.02	0.75	0.22	0.40	1.7×10^{-6}	2.8×10^{-6}
NSC-2	0.25 ± 0.01	0.70	0.21	0.39	3.9×10^{-6}	8.7×10^{-6}
NSC-3	0.28 ± 0.02	0.77	0.18	0.51	1.7×10^{-5}	2.6×10^{-5}
NSC-4	0.30 ± 0.02	0.54	0.22	0.30	2.5×10^{-6}	7.6×10^{-7}
NSC-5	0.40 ± 0.04	0.47	0.23	0.23	5.2×10^{-6}	5.7×10^{-7}
NSC-6	0.46 ± 0.04	0.62	0.27	0.31	5.1×10^{-6}	1.6×10^{-7}
Substrate 100Cr6	0.75 ± 0.06	1.01	0.46	0.75	6.0×10^{-5}	3.1×10^{-5}

It was concluded that the NSC surface roughness (Table 2) did not significantly affect the friction coefficient in the examined experimental settings. Although, if the NSC surface roughness noticeably increased (in this study, up to Sa 0.2 μm), a tribolayer could form on NSC films, which resulted in a friction coefficient and wear rate increase [24]. In this study, the wear rate increased as the surface roughness increased for the Hf-doped samples (NSC-1, NSC-2, and NSC-3), but more detailed analysis is necessary to confirm the correlation. However, similar findings are reported in the known literature. For example, Kubiak et al. [25] studied the roughness influence on wear properties using AISI1034 and titanium alloy materials. The roughness influence on tribological properties was also analyzed by Ghosh et al. [26]. A WC-Co coating was sprayed on low-carbon steel and then three surfaces were compared: sprayed, grounded, and nano-finished. It was observed that surface roughness decreased linearly related to the wear rate decrease. A similar trend has also been observed in studies using magnetron sputtering. In Svahn et al.'s study [27], tungsten- and chromium-containing coatings were deposited on 100Cr6 substrates with different surface roughness. It was concluded that a higher surface roughness increases the wear rate as well as the friction coefficient. Hanief et al. [28] studied EN-31 steel material. Their study mathematically and experimentally demonstrated that the wear rate increased as the surface roughness parameter Ra (ranging from 0.2 to 1.2 μm) increased. Samples with the Nb dopant (NSC-4, NSC-5, and NSC-6) had a similar surface roughness and wear rate. An effect on friction or wear properties by reducing the substrate hardness was not noticed in the examined experimental settings.

Taking into account the measured wear rates (see Table 3), as well as analyzing the wear for both the ball specimen and the coating (see Appendices A and B), it is likely that the wear process of the Hf-doped coatings (NSC-1–NSC-3) consists of classic abrasive and polishing wear, which is affected by carbon diffusion [29]. The friction coefficient curves confirmed this (see Appendix D, Figure A3). At first, asperities of the coating film attempt to penetrate the softer counter surface, resulting in a plastic flow of material around the coated surface. Then, counter surface particles promote abrasive friction, increasing frictional forces and the temperature between both surfaces. As a result, an increase in carbon diffusion weakens the coated surface asperities, resulting in micro-cleavage. Then, an increase in carbon diffusion reduces the atomic bond strength, which results in micro-cleavage in polishing wear. As a result, the friction coefficient decreases. A further increase in carbon diffusion implies a weakening of the coated film, and the surface remains smoother. Counter surface strengthening and coated surface smoothness result in the stabilization of the friction coefficient [29]. For Nb-doped coatings (NSC-4–NSC-6), a similar pattern appeared, but at a shorter distance (from 5 to 20 m), and then the friction coefficient curve increased and stabilized (see Appendix D, Figure A4). A similar result was shown in Madej's research [30], where it was explained that the chemical composition and structure of the interlayer materials significantly influence tribological properties. Additionally, the coating thickness and the thickness of the layers could affect the tribological properties. In Sidiqui et al.'s work [31], it was concluded that the thickness of the coating layers affected the effective diffusion of nitrogen into the surface, leading to

a compositionally and microstructurally heterogeneous subsurface layer. As a result, the hard and brittle coating was broken on the softened substrate, producing hard-wear debris particles and leading to severe wear due to a three-body abrasive wear mechanism. It was noticed that for Nb-doped coatings, all ball specimens had a smaller wear area diameter than the width of the wear track (see Appendices A and B), which was also indicated by the wear rates in Table 3. This suggests that loose particles affect the wear process. On the other hand, for Hf-doped coatings, a lower specific wear rate (see Table 3) and a lower width of the wear track were observed compared to the ball specimen wear area diameter (see Appendices A and B). In future research, nitriding of the substrate could be performed, thus improving the coatings' wear properties and overall lifespan [32].

3.2.3. Micromechanical Properties

The adhesion test (DIN 4856: 2018-02) was used to determine the adhesion of the deposited NSC samples. Figure 4 shows indentation crater segments after the adhesion test. All results correspond to the HF1 and HF2 classes, which indicate the acceptable adhesion of the coating. Additionally, substrate hardness (in the Rockwell HRC scale) was clarified during these measurements, and obtained values are shown in Table 4.
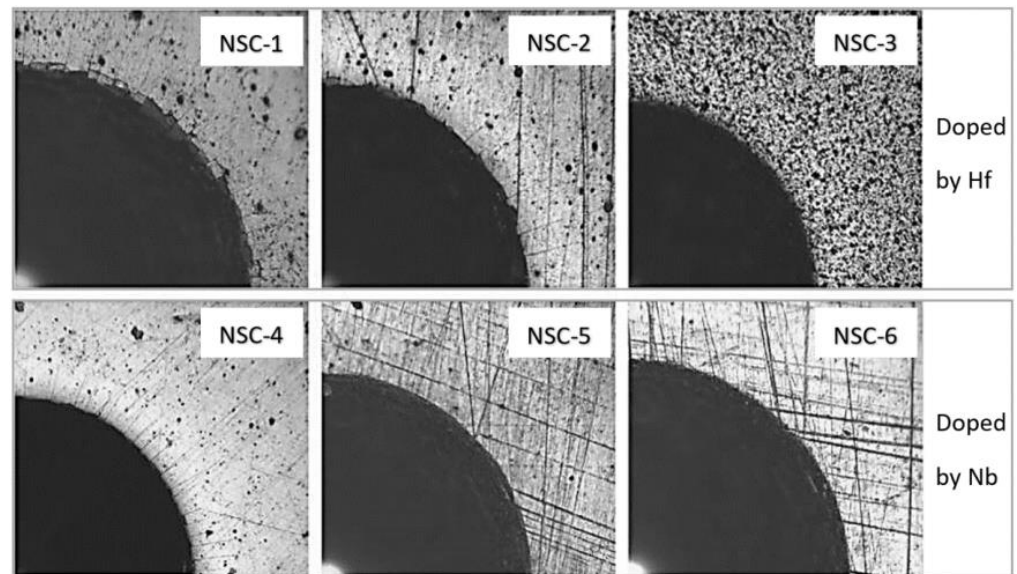
Figure 4. Adhesion assessment of the NSC samples by the Rockwell indentation hardness using the Rockwell C-scale, i.e., by the HRC test. The 90° sectors of the HRC test imprints are shown to demonstrate the coating's adhesion according to DIN 4856: 2018-02.

Micromechanical properties were mainly analyzed using microhardness measurements (micro-Vickers). Micro-indentation was used instead of nanoindentation because it is less sensitive to the effect of surface texture than nanoindentation. Following the recommendations of the standard ISO 14577-1:2015 (Metallic materials—Instrumented indentation test for hardness and materials' parameters—Part 1: Test method), the surface roughness parameter, Ra, should be less than 5% of the maximum indentation depth. In this case, the coating surface roughness exceeded this value if indentations were made using test forces lower than 0.1 N. Thus, traditional nanoindentation, where the applied force varies from a few micro-newtons to about 0.2 N [33], was unreliable. Samples with an Rz (see Table 2) value higher than the indentation depth, at the lowest applied force (see Table 4 (displacement into surface at a 0.1 N applied test force)), also showed a possible intermediate effect of the surface texture on the measurement result. For example, in Bohme's study [34], a polished surface (Ra 2–3 nm) and a milled surface with traces of machining (Ra 126–240 nm) were compared. Results indicated that the surface with a higher surface roughness showed higher microhardness values, and the measurement error

significantly increased (over 40%), highlighting the significant surface preparation impact on microhardness measurements. Additionally, in our study, the standard deviation of microhardness measurements increased for NSC samples with a higher surface roughness (see Table 4 and Appendix C). However, microhardness value measurements at a 0.1 N applied force showed acceptable deviation (less than ±75 HV).

The microhardness was measured for each NSC sample in the test force range from 0.10 (lowest technologically possible) to 6.88 N. The shown measurement value for each applied force was calculated as the average value from ten measurements (see the test matrix sketch in Figure 1). Table 4 includes only microhardness values obtained at a 0.1 N applied test force because this value most reliably corresponds to NSC hardness. All other microhardness measurements and standard deviations for all used test forces are shown in Appendix C Table A1. The microhardness tester used also provided information on indenter displacement into the surface during each indent (see graphical representation in Figure 5). This information was used to understand whether indentation did not exceed the coating thickness and was used in the preparation of the graph (see Figures 6 and 7). The standard deviation bars in Figures 6 and 7 are not visible because they are smaller than the marker point, but standard deviation values are shown in Table 4 and Appendix C.

Table 4. Overview of the NSC micromechanical properties.

Sample Label	Coating Thickness (nm)	Microhardness (HV (0.1 N))	Displacement Into Surface (µm (0.1 N))	Substrate Hardness (HRC)	Adhesion by HRC Test
NSC-1	~4800	2650 ± 16	0.7 ± 0.05	54 ± 2	HF2
NSC-2	~6300	3205 ± 43	0.6 ± 0.06	19 ± 1	HF1
NSC-3	~6200	2844 ± 75	0.6 ± 0.04	14 ± 1	HF1
NSC-4	~4200	2168 ± 27	0.5 ± 0.04	19 ± 1	HF1
NSC-5	~3400	1719 ± 8	0.8 ± 0.04	59 ± 2	HF1
NSC-6	~2300	1777 ± 14	0.5 ± 0.05	57 ± 2	HF1
Substrate 100Cr6		967 ± 12	1.2 ± 0.06	58 ± 2	N/A

Figures 6 and 7 show NSC sample microhardness measurement values. The graph is divided into three parts: coating microhardness, integrated microhardness (coating + substrate), and substrate microhardness. A graphical explanation for why these three parts were separated is shown in Figure 5. In the coating microhardness part, the indentation depth did not exceed 10% of the coating thickness. In this case, the substrate had minimal or no effect on the obtained hardness value [35]. In the integrated microhardness part, the indentation depth was between 10% and 100% of the coating thickness, so the influence of the substrate was noticeable and increased at a more profound indentation depth. In the substrate microhardness part, the indenter had fully penetrated through the coating, and the observed hardness values approached the substrate hardness value.
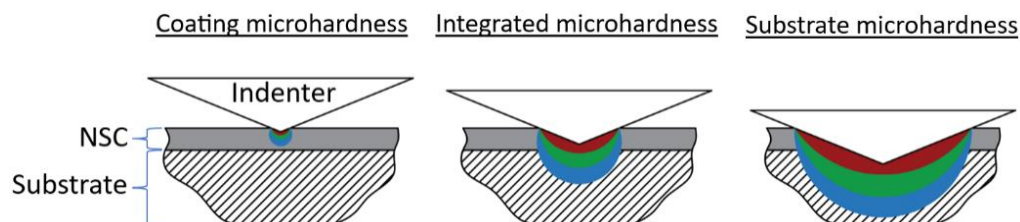
Figure 5. Graphical representation of micro-indentation depths: coating microhardness, integrated microhardness, and substrate microhardness. Colored curves represent internal stress in the material caused by the micro-Vickers indenter.

In Figure 6, where the microhardness of samples with the Hf dopant is shown, the NSC-1 (red markers) was deposited on a harder 100Cr6 substrate (HRC 54), but the coatings on samples NSC-2 (blue markers) and NSC-3 (green markers) were deposited on a softer

substrate (HRC 14–19). As seen in the graph (Figure 6), even with the lowest available indentation force of 0.1 N, the indenter still penetrated deeper than 10% of the coating thickness, disturbing the reliable analysis of the coating hardness without considering the effect of the substrate. Therefore, the absolute hardness values of the coatings could be higher. So-called coating true hardness (without substrate influence) could be calculated using known mathematical models [36] but would require more experimental data, i.e., more indentations over a broader load range, and would need to make sure that the data are correctly interpreted because of the hardness of the substrate and its effect on the measurement values. It can be seen that the absolute microhardness values of NSC samples doped with Hf reached 3000 HV. The highest microhardness was observed for NSC-2 and NSC-3 samples with thicker coating layers. Therefore, taking into account that the results of micro-indentation were practically in the integrated microhardness range, it is possible that at a relatively small displacement into the surface (up to 0.8 μm), the influence of the substrate on the result was lower for samples NSC-2 and NSC-3 due to their thicker coating layers. When displacement into the surface exceeded 1.6 micrometers, samples NSC-2 and NSC-3 showed a rapid decrease in microhardness, compared to NSC-1, which was deposited on a harder substrate, highlighting the substrate hardness influence on the results. The softer the substrate, the more rapidly the microhardness decreased if the indentation depth increased. For sample NSC-1, the curve was flatter, and the transition from coating microhardness to substrate microhardness was more gradual. If the NSC-1 coating thickness was higher, the maximal observed microhardness value was also expected to be higher.
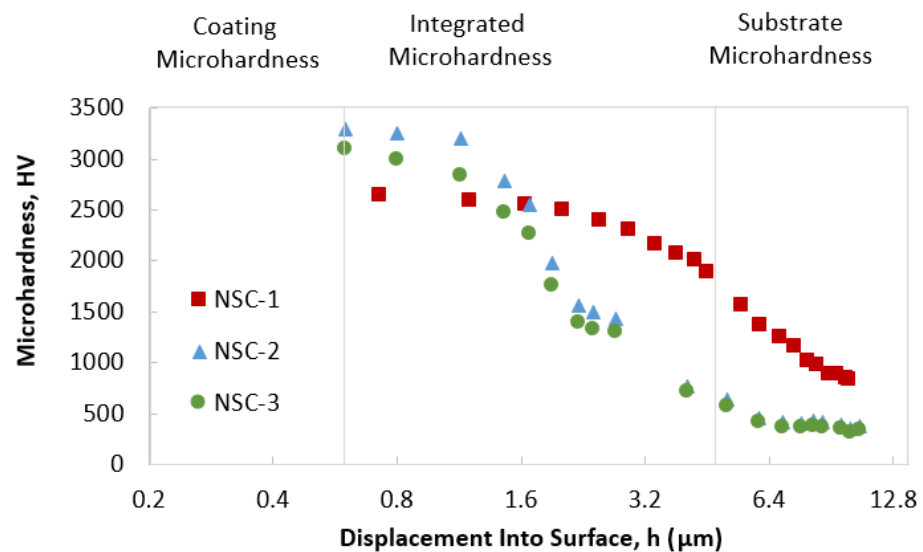
Figure 6. Microhardness dependence on displacement into the surface for the NSC samples doped with atomic element Hf (NSC-1—red, NSC-2—blue, NSC-3—green). The graph is divided into three parts characterizing coating microhardness, integrated microhardness, and substrate microhardness.

Figure 7 shows the microhardness values of samples doped with Nb. Additionally, this graph is divided into three zones, following the same methodology described above.

These samples had a broader coating thickness variation ranging from 2300 nm for NSC-6 (grey marker) to 4200 nm for NSC-4 (black marker). The NSC-4 was deposited on a softer 100Cr6 substrate (19 HRC), but the NSC-5 (orange marker) and NSC-6 were deposited on a harder substrate (57–59 HRC).
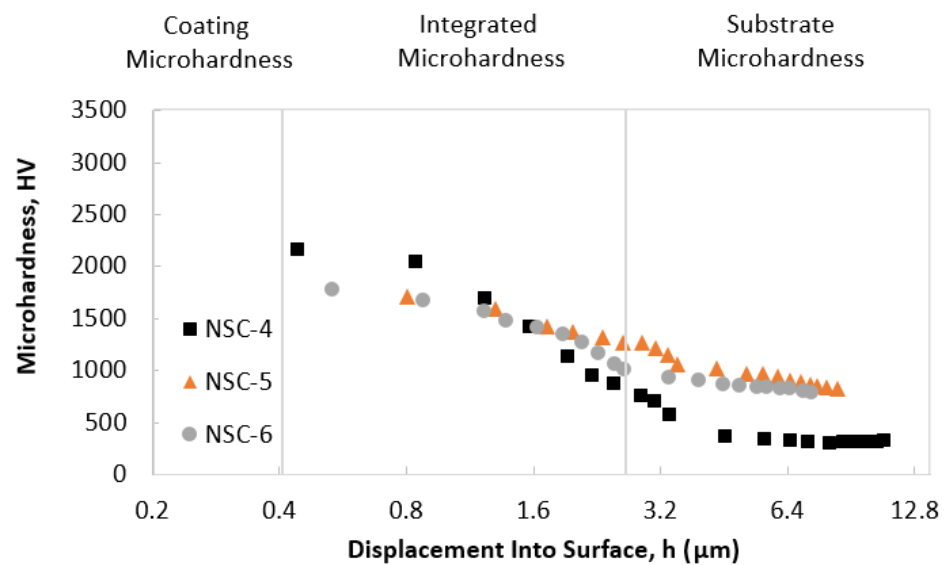
Figure 7. Microhardness dependence on displacement into the surface for the NSC samples doped with atomic element Nb (NSC-4—black, NSC-5—orange, NSC-6—grey). The graph is divided into three parts characterizing coating microhardness, integrated microhardness, and substrate microhardness.

Results show that coatings doped with Nb provided microhardness values up to 2000 HV. The highest microhardness value was observed for the sample NSC-4, which had the thickest coating layer, similar to the case of NSC-2 and NSC-3 in Figure 6. The trends of the curves in both graphs (Figures 6 and 7) are similar, i.e., the coatings that were deposited on the harder substrate showed a smoother transition in the integrated microhardness zone, while the coatings applied on the softer substrate showed a rapid decrease in microhardness values when the indentation depth exceeded half of the coating thickness.

Although it was difficult to accurately determine the coatings' absolute hardness values using the micro-indentation method, it was possible to observe that the NSC coating noticeably increased the surface microhardness. Hardness for coatings doped with Hf exceeded 3000 HV, while coatings doped with Nb had a 2000 HV surface hardness. It was also found that the microhardness of the coatings on the softer substrate reduced faster than those on the harder substrate if higher indentation loads were used.

For future studies, substrate surface roughness will be significantly reduced to ensure that nanoindentation measurements with lower displacement into the surface are possible. Additionally, more experiments with the microhardness indenter will be performed and the obtained data will be used to develop mathematical modeling of the microhardness prediction of coatings. Such a prediction model will be critically important for all researchers who do not have access to a nano-indenter but have a microhardness testing machine.

4. Conclusions

The above-noted general empirical formula for modified non-stoichiometric carbonitride/nitride bilayer Ti*Me*-CN/TiAlSi-N, where *Me* = Hf or Nb, manifested high wear resistance (up to 35× improvement in the case of Hf-doped and up to 24× improvement in the case of Nb-doped against 100Cr6 substrate material), a lower friction coefficient (up to 3× reduction in the case of Hf-doped, and up to 2.5× reduction in the case of Nb-doped against 100Cr6 substrate material), and a high coating hardness (up to 3.8× increase in the case of Hf-doped, and up to 2.6× increase in the case of Nb-doped against 100Cr6 substrate material).

Micro-indentation hardness tests in the applied force range from 0.10 to 6.88 N provided data for analyzing the integrated microhardness of NSC samples. The measured values were highly dependent on the thickness of the coatings and the substrate hard-

ness. In the low applied force range (0.10–0.29 N), the coatings with a higher thickness had higher microhardness values. A softer NSC substrate resulted in a steeper drop in microhardness values, with increasing displacement into the surface compared to a higher hardness substrate.

It was found that the hardness of the substrate did not directly affect the tribological properties in the considered tribology experiment setting range, while the surface texture noticeably affected the wear properties. A higher NSC surface roughness resulted in a higher specific wear rate.

In order to more accurately evaluate the hardness, in the future research, additional experiments using micro-indentation and nanoindentation methods will be performed. Consequently, a mathematical model for the prognosis of the coatings' hardness using microhardness will be developed.

Author Contributions: Conceptualization, A.L., U.K., J.L., E.J., K.K., I.B., O.L., and V.K.; investigation, A.L., U.K., E.J., J.L., K.K., V.K., and O.L.; writing—original draft preparation, A.L. and U.K.; writing—review and editing, A.L., U.K., E.J., J.L., and I.B.; visualization, A.L., E.J., J.L., U.K., and K.K.; supervision I.B.; project administration I.B.; funding acquisition I.B. All authors have read and agreed to the published version of the manuscript.

Funding: This research was funded by the Latvian Council of Science, project "Carbon-rich self-healing multifunctional nanostructured smart coatings (NSC) for high-tech applications using high-power confined plasma technology for their deposition", project No. 2019/1-0385.

Institutional Review Board Statement: Not applicable.

Informed Consent Statement: Not applicable.

Data Availability Statement: The data presented in this study are available on request from the corresponding author.

Acknowledgments: The authors thank Mitutoyo Poland Sp.o.o. for providing access to a micro-Vickers hardness testing machine HM-210D.

Conflicts of Interest: The authors declare no conflict of interest.

Appendix A
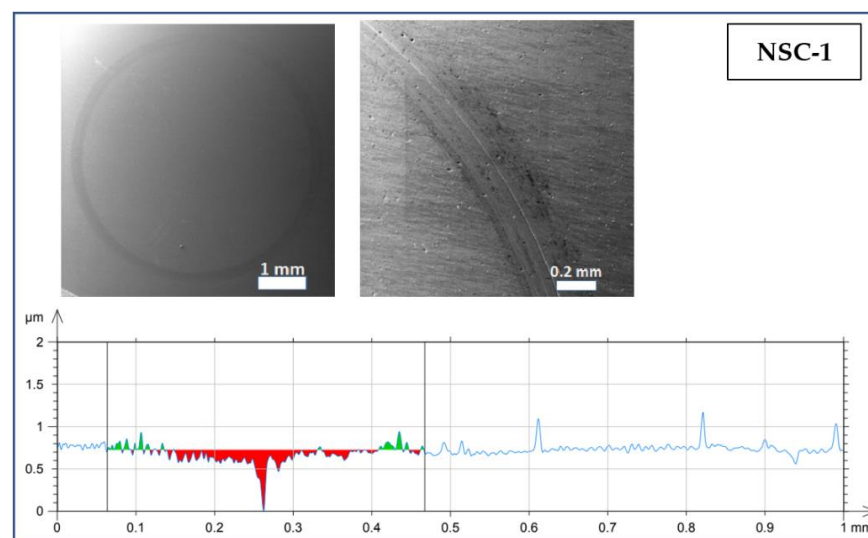
Figure A1. *Cont.*
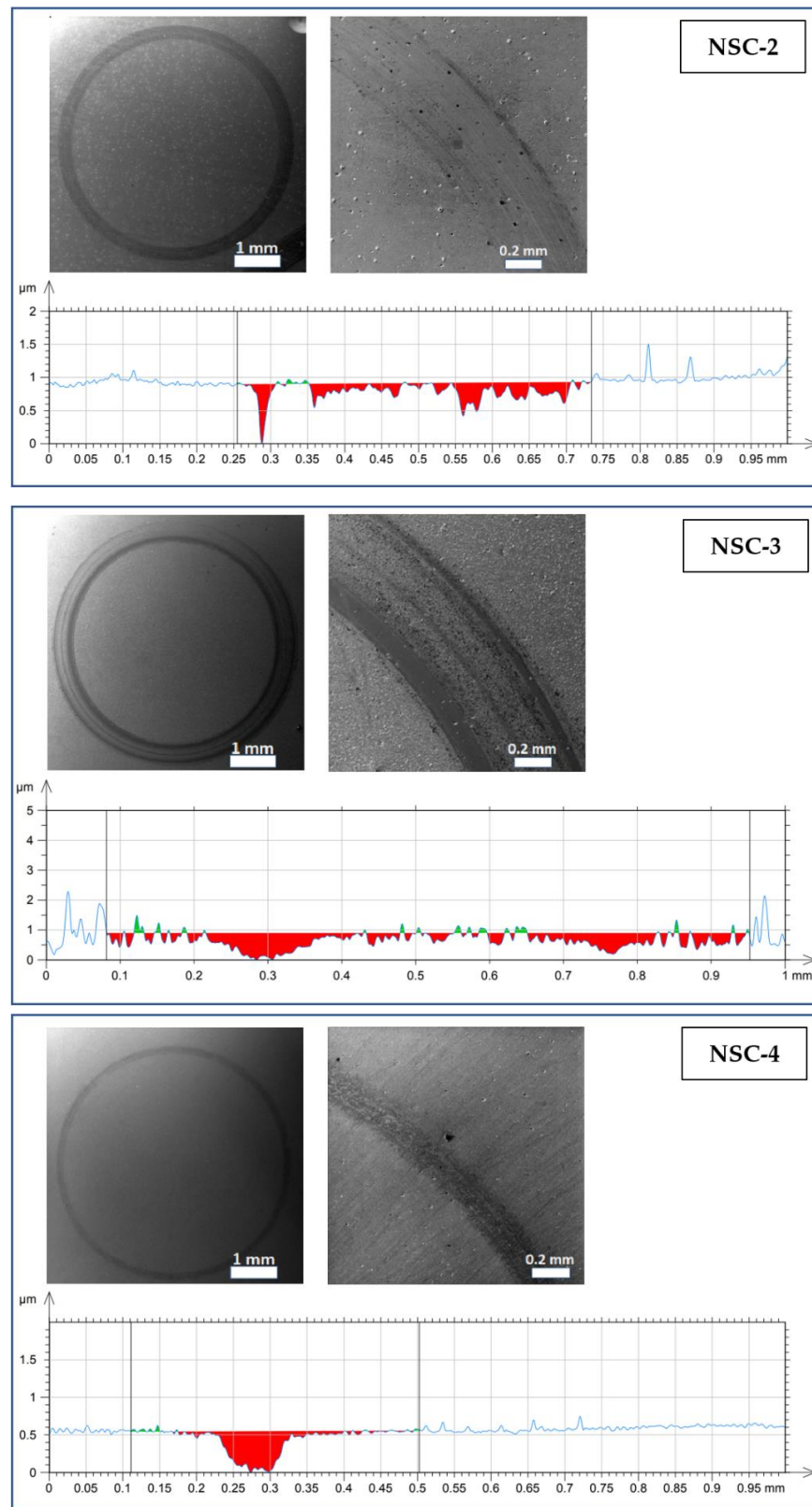
Figure A1. *Cont.*
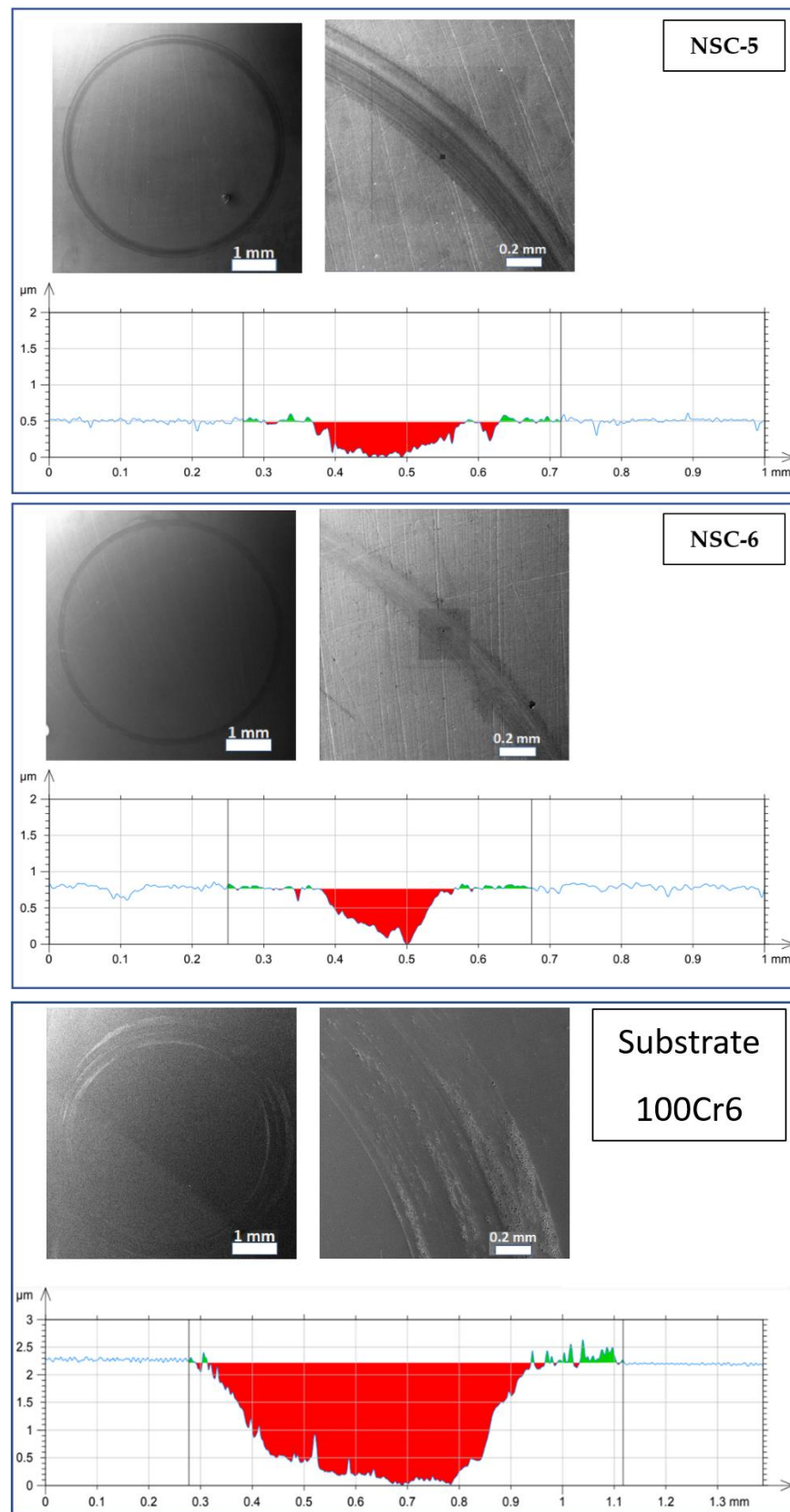
Figure A1. Wear track SEM images and cross-sectional profiles for NSC coatings and substrate 100Cr6. Top left: wear track SEM overview, Top right: wear track SEM closeup, Bottom: wear track cross-sectional profile.

Appendix B

NSC-1
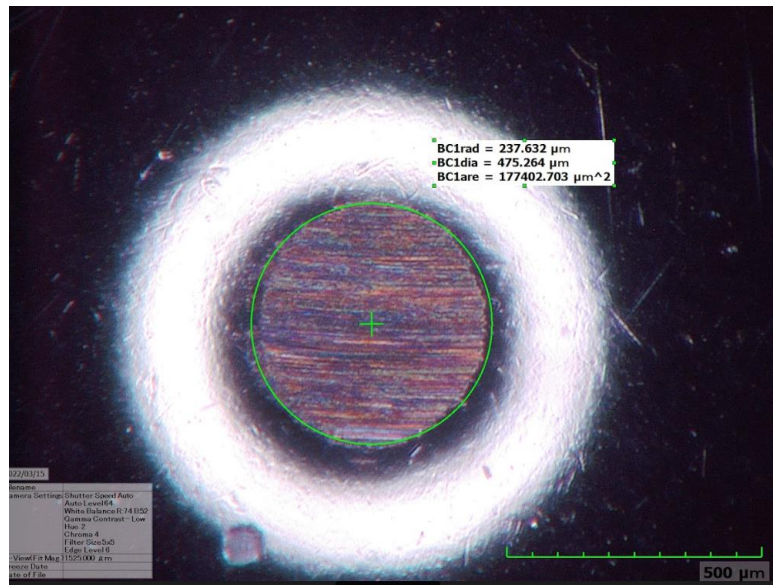
NSC-2
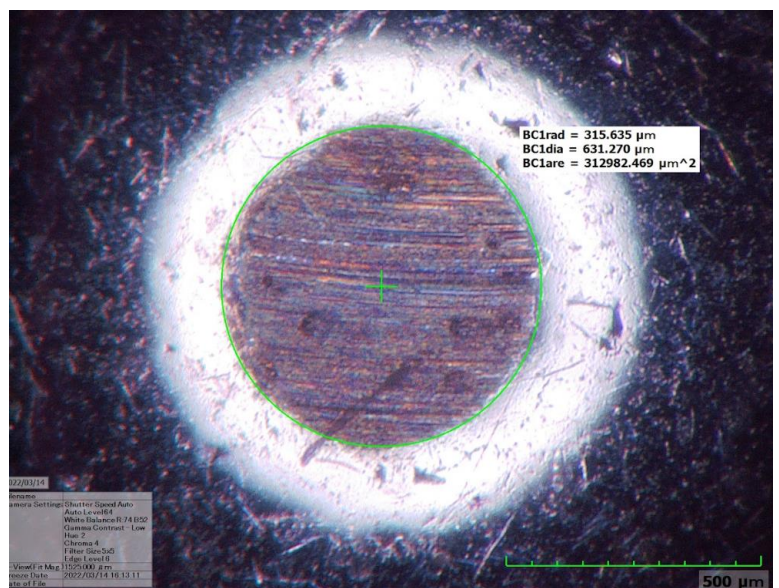
Figure A2. *Cont*.

NSC-3
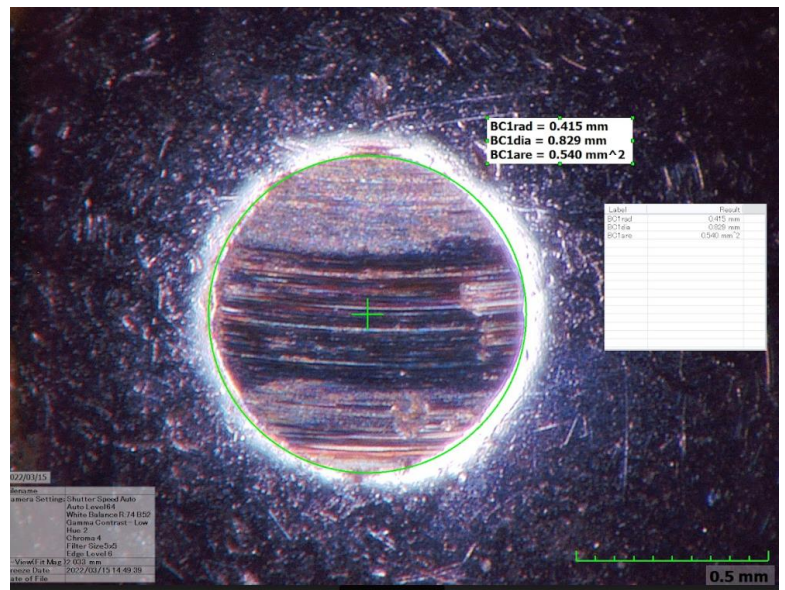
NSC-4
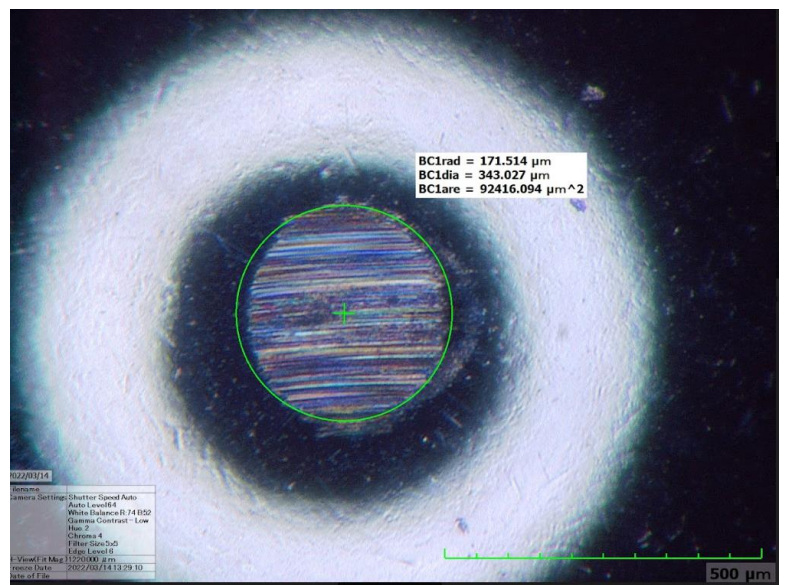
Figure A2. *Cont.*

NSC-5
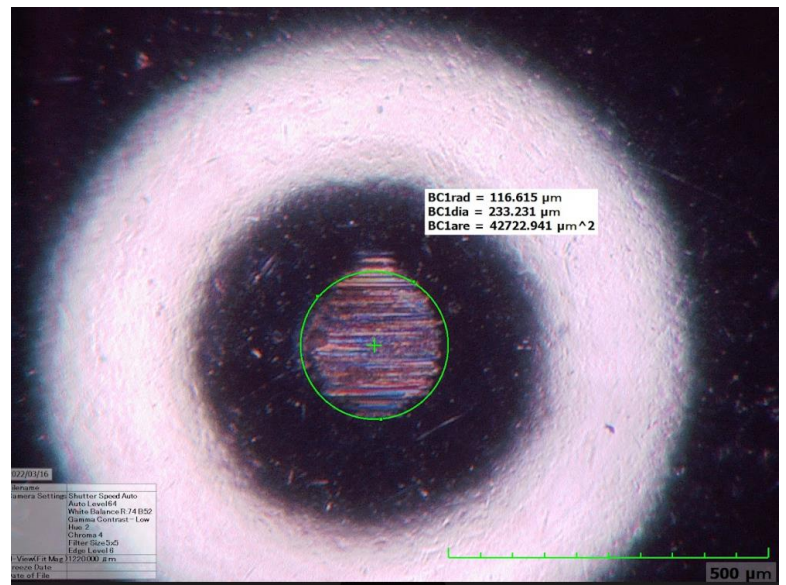
NSC-6
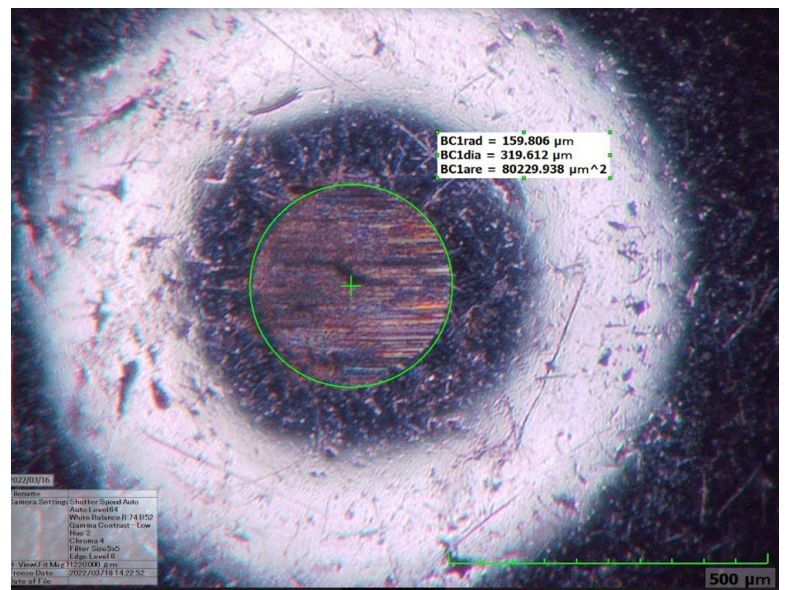
Figure A2. *Cont.*

Substrate 100Cr6
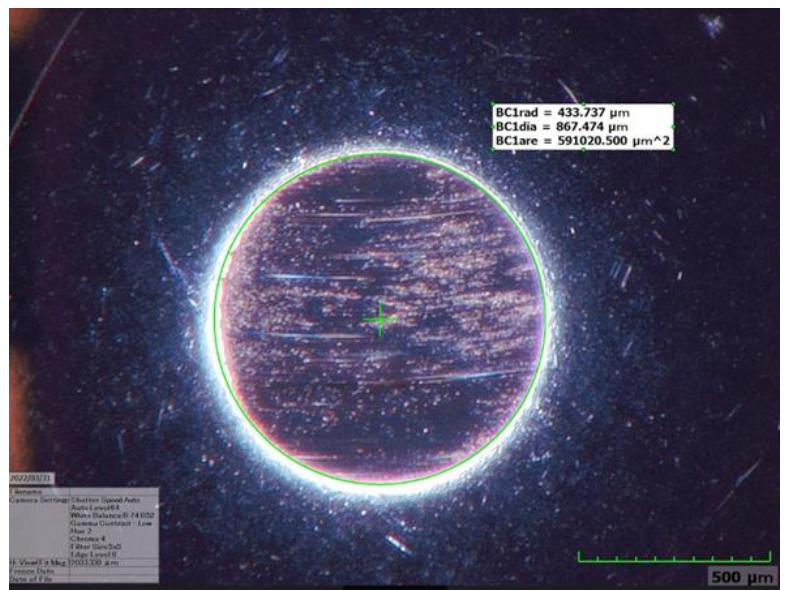
Figure A2. Ball specimen (100Cr6) worn surface after tribological tests.

Appendix C

Table A1. Microhardness measurement values.

Test Force, N	NSC-1, HV	NSC-2, HV	NSC-3, HV	NSC-4, HV	NSC-5, HV	NSC-6, HV	Substrate 100Cr6, HV
0.10	2650 ± 16	3300 ± 43	3100 ± 75	2168 ± 27	1719 ± 8	1777 ± 14	967 ± 5
0.20	2595 ± 22	3255 ± 44	3000 ± 66	2049 ± 28	1596 ± 27	1670 ± 19	931 ± 5
0.29	2557 ± 16	3205 ± 37	2844 ± 62	1696 ± 35	1430 ± 29	1566 ± 15	898 ± 2
0.39	2495 ± 20	2783 ± 42	2469 ± 53	1421 ± 11	1371 ± 17	1473 ± 21	883 ± 2
0.49	2393 ± 24	2552 ± 48	2264 ± 66	1142 ± 62	1319 ± 8	1408 ± 10	
0.59	2312 ± 23	1977 ± 58	1754 ± 63	959 ± 20	1269 ± 28	1344 ± 7	872 ± 7
0.69	2162 ± 43	1569 ± 34	1392 ± 37	887 ± 18	1271 ± 16	1266 ± 7	
0.78	2070 ± 23	1503 ± 23	1333 ± 33	763 ± 31	1224 ± 5	1165 ± 18	862 ± 7
0.88	2009 ± 43	1437 ± 16	1300 ± 31	713 ± 14	1153 ± 12	1064 ± 19	
0.98	1892 ± 25	770 ± 16	720 ± 21	586 ± 30	1067 ± 25	1013 ± 23	861 ± 12
1.47	1563 ± 36	634 ± 23	580 ± 39	377 ± 30	1020 ± 22	938 ± 3	
1.96	1374 ± 42	461 ± 42	420 ± 28	353 ± 11	978 ± 8	909 ± 10	833 ± 23
2.45	1245 ± 24	419 ± 18	372 ± 17	340 ± 5	974 ± 5	867 ± 32	
2.94	1167 ± 11	410 ± 10	364 ± 18	319 ± 5	943 ± 13	855 ± 5	828 ± 24
3.43	1013 ± 12	427 ± 6	379	309 ± 4	905 ± 3	845 ± 5	
3.92	978 ± 18	413 ± 14	366 ± 13	315 ± 4	888 ± 6	835 ± 6	809 ± 7
4.41	885 ± 5	393 ± 12	349 ± 16	326 ± 3	866 ± 11	832 ± 4	
4.90	887 ± 2	357 ± 10	317 ± 12	320 ± 13	854 ± 2	829 ± 3	794 ± 3
5.39	843 ± 3	379 ± 17	336 ± 15	319 ± 2	840 ± 6	799 ± 10	
5.88	840 ± 3	376 ± 15	342 ± 11	330 ± 1	824 ± 9	792 ± 7	800 ± 7

Appendix D
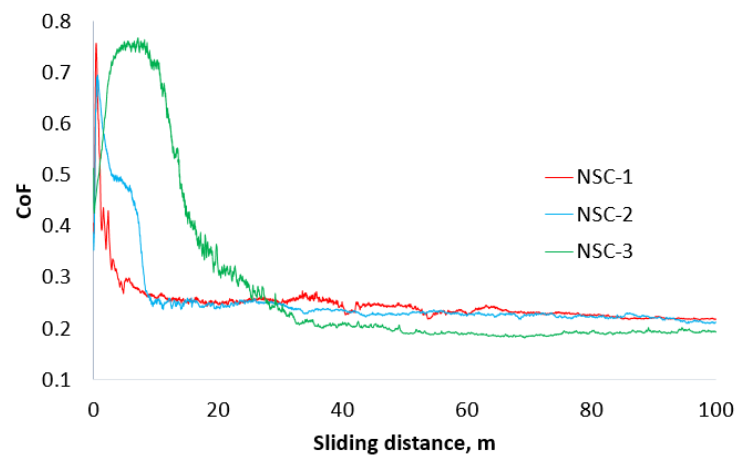
Figure A3. CoF curves for Hf-doped samples.
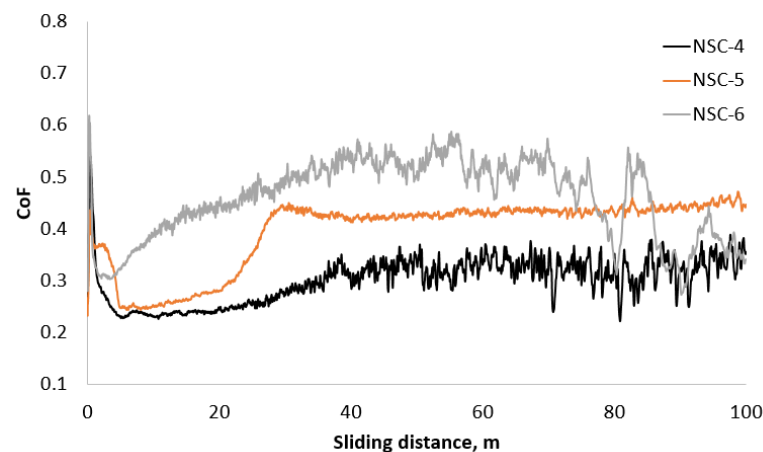
Figure A4. CoF curves for Nb-doped samples.

References

1. Musil, J.; Vlček, J. Magnetron Sputtering of Hard Nanocomposite Coatings and Their Properties. *Surf. Coat. Technol.* **2001**, *142–144*, 557–566. [CrossRef]
2. Musil, J. Hard and Superhard Nanocomposite Coatings. *Surf. Coat. Technol.* **2000**, *125*, 322–330. [CrossRef]
3. Zhang, S.; Sun, D.; Fu, Y.; Du, H. Recent Advances of Superhard Nanocomposite Coatings: A Review. *Surf. Coat. Technol.* **2003**, *167*, 113–119. [CrossRef]
4. Chang, Y.Y.; Lai, H.M. Wear Behavior and Cutting Performance of CrAlSiN and TiAlSiN Hard Coatings on Cemented Carbide Cutting Tools for Ti Alloys. *Surf. Coat. Technol.* **2014**, *259*, 152–158. [CrossRef]
5. Miletić, A.; Panjan, P.; Škorić, B.; Čekada, M.; Dražič, G.; Kovač, J. Microstructure and Mechanical Properties of Nanostructured Ti–Al–Si–N Coatings Deposited by Magnetron Sputtering. *Surf. Coat. Technol.* **2014**, *241*, 105–111. [CrossRef]
6. Wu, W.Y.; Ting, J.M. Growth and Characteristics of Metal-Containing Diamond-like Carbon Using a Self-Assembled Process. *Carbon* **2006**, *44*, 1210–1217. [CrossRef]
7. Persson, K.; Gåhlin, R. Tribological Performance of a DLC Coating in Combination with Water-Based Lubricants. *Tribol. Int.* **2003**, *36*, 851–855. [CrossRef]
8. Das, J.; Linke, B. Evaluation and Systematic Selection of Significant Multi-Scale Surface Roughness Parameters (SRPs) as Process Monitoring Index. *J. Mater. Process. Technol.* **2017**, *244*, 157–165. [CrossRef]
9. Pogrebnjak, A.; Smyrnova, K.; Bondar, O. Nanocomposite Multilayer Binary Nitride Coatings Based on Transition and Refractory Metals: Structure and Properties. *Coatings* **2019**, *9*, 155. [CrossRef]
10. Das, P.; Anwar, S.; Bajpai, S.; Anwar, S. Structural and Mechanical Evolution of TiAlSiN Nanocomposite Coating under Influence of Si3N4 Power. *Surf. Coat. Technol.* **2016**, *307*, 676–682. [CrossRef]
11. Liu, Y.; Yu, S.; Shi, Q.; Ge, X.; Wang, W. Multilayer Coatings for Tribology: A Mini Review. *Nanomaterials* **2022**, *12*, 1388. [CrossRef] [PubMed]

12. Kanders, U.; Lungevics, J.; Leitans, A.; Boiko, I.; Berzins, K.; Trubina, Z. Nanostructured TiAlSi-CN:Me/a-CN:Si3N4 Composite Coatings Deposited by Advanced PVD Technique. *Solid State Phenom.* **2021**, *320*, 37–42. [CrossRef]

13. Leitans, A.; Lungevics, J.; Kanders, U.; Boiko, I. Micromechanical and Tribological Properties of Nanostructured Carbonitride Coatings Deposited by PVD Technique. *Key Eng. Mater.* **2021**, *903*, 177–182. [CrossRef]

14. Maniks, J.; Mitin, V.; Kanders, U.; Kovalenko, V.; Nazarovs, P.; Baitimirova, M.; Meija, R.; Zabels, R.; Kundzins, K.; Erts, D. Deformation Behavior and Interfacial Sliding in Carbon/Copper Nanocomposite Films Deposited by High Power DC Magnetron Sputtering. *Surf. Coat. Technol.* **2015**, *276*, 279–285. [CrossRef]

15. Münz, W.D.; Donohue, L.A.; Hovsepian, P.E. Properties of Various Large-Scale Fabricated TiAlN- and CrN-Based Superlattice Coatings Grown by Combined Cathodic Arc–Unbalanced Magnetron Sputter Deposition. *Surf. Coat. Technol.* **2000**, *125*, 269–277. [CrossRef]

16. Maiti, R.; Mills, R. Wear Properties of Diamond-like-Carbon Coatings with Silicon and Chromium as Adhesion Layer Using a High Frequency Reciprocating Rig. *Proc. Inst. Mech. Eng. Part J-J. Eng. Tribol.* **2017**, *231*, 1605–1615. [CrossRef]

17. Sedlaček, M.; Podgornik, B.; Vižintin, J. Tribological Properties of DLC Coatings and Comparison with Test Results: Development of a Database. *Mater. Charact.* **2008**, *59*, 151–161. [CrossRef]

18. Khun, N.W.; Lee, P.M.; Toh, W.Q.; Liu, E. Tribological Behavior of Nickel-Doped Diamond-Like Carbon Thin Films Prepared on Silicon Substrates via Magnetron Sputtering Deposition. *Tribol. Trans.* **2016**, *59*, 845–855. [CrossRef]

19. Vicen, M.; Bronček, J.; Nový, F. Investigation of Tribological Properties of CarbonX Coating Deposited on 100Cr6 Steel. *Prod. Eng. Arch.* **2019**, *25*, 52–55. [CrossRef]

20. Boiko, I.; Kanders, U.; Kundzins, K.; Leitans, A.; Lungevičs, J.; Jansons, E.; Linins, O. Nanostructured Smart Coatings Obtained by the High Power Magnetically Compresed Plasma Method. In Proceedings of the RTU 63rd International Scientific Conference Section Mechanical Engineering Technology and Heat Engineering, Riga, Latvija, 14 October 2022; RTU Press: Riga, Latvija, 2023; pp. 19–21.

21. Vossen, J.L. *Thin Film Processes*, 1st ed.; Elsevier Science: Amsterdam, The Netherlands, 1978; ISBN 9780323138987.

22. Pawlus, P.; Reizer, R.; Wieczorowski, M. Functional Importance of Surface Texture Parameters. *Materials* **2021**, *14*, 5326. [CrossRef]

23. Linins, O.; Jansons, E.; Leitans, A.; Boiko, I.; Lungevics, J. Estimation of Service Life of Mechanical Engineering Components. *Key Eng. Mater.* **2019**, *799*, 71–76. [CrossRef]

24. Soprano, P.B.; Salvaro, D.B.; Giacomelli, R.O.; Binder, C.; Klein, A.N.; de Mello, J.D.B. Effect of Soft Substrate Topography on Tribological Behavior of Multifunctional DLC Coatings. *J. Brazilian Soc. Mech. Sci. Eng.* **2018**, *40*, 371. [CrossRef]

25. Kubiak, K.J.; Liskiewicz, T.W.; Mathia, T.G. Surface Morphology in Engineering Applications: Influence of Roughness on Sliding and Wear in Dry Fretting. *Tribol. Int.* **2011**, *44*, 1427–1432. [CrossRef]

26. Ghosh, G.; Sidpara, A.; Bandyopadhyay, P.P. Understanding the Role of Surface Roughness on the Tribological Performance and Corrosion Resistance of WC-Co Coating. *Surf. Coat. Technol.* **2019**, *378*, 125080. [CrossRef]

27. Svahn, F.; Kassman-Rudolphi, Å.; Wallén, E. The Influence of Surface Roughness on Friction and Wear of Machine Element Coatings. *Wear* **2003**, *254*, 1092–1098. [CrossRef]

28. Hanief, M.; Wani, M.F. Effect of Surface Roughness on Wear Rate during Running-in of En31-Steel: Model and Experimental Validation. *Mater. Lett.* **2016**, *176*, 91–93. [CrossRef]

29. Tyagi, A.; Walia, R.S.; Murtaza, Q.; Pandey, S.M.; Tyagi, P.K.; Bajaj, B. A Critical Review of Diamond like Carbon Coating for Wear Resistance Applications. *Int. J. Refract. Met. Hard Mater.* **2019**, *78*, 107–122. [CrossRef]

30. Madej, M. The Effect of TiN and CrN Interlayers on the Tribological Behavior of DLC Coatings. *Wear* **2014**, *317*, 179–187. [CrossRef]

31. Siddiqui, S.A.; Maros, M.B.; Pakseresht, A.; Kirubaharan, K.; Mosas, A.; Siddiqui, S.A.; Maros, M.B. Comparative Study on the Scratch and Wear Resistance of Diamond-like Carbon (DLC) Coatings Deposited on X42Cr13 Steel of Different Surface Conditions. *Ceramics* **2022**, *5*, 1207–1224. [CrossRef]

32. Özkan, D.; Alper Yilmaz, M.; Karakurt, D.; Szala, M.; Walczak, M.; Atas, S.B.; Türküz, C.; Sulukan, E. Effect of AISI H13 Steel Substrate Nitriding on AlCrN, ZrN, TiSiN, and TiCrN Multilayer PVD Coatings Wear and Friction Behaviors at a Different Temperature Level. *Materials* **2023**, *16*, 1594. [CrossRef]

33. Broitman, E. Indentation Hardness Measurements at Macro-, Micro-, and Nanoscale: A Critical Overview. *Tribol. Lett.* **2017**, *65*, 23. [CrossRef]

34. Böhme, L.; Keksel, A.; Ströer, F.; Bohley, M.; Kieren-Ehses, S.; Kirsch, B.; Aurich, J.C.; Seewig, J.; Kerscher, E. Micro Hardness Determination on a Rough Surface by Using Combined Indentation and Topography Measurements. *Surf. Topogr. Metrol. Prop.* **2019**, *7*, 045021. [CrossRef]

35. Chen, K.S.; Chen, T.C.; Ou, K.S. Development of Semi-Empirical Formulation for Extracting Materials Properties from Nanoindentation Measurements: Residual Stresses, Substrate Effect, and Creep. *Thin Solid Films* **2008**, *516*, 1931–1940. [CrossRef]

36. Wei, Z.; Zhang, G.; Chen, H.; Luo, J.; Liu, R.; Guo, S. A Simple Method for Evaluating Elastic Modulus of Thin Films by Nanoindentation. *J. Mater. Res.* **2009**, *24*, 801–815. [CrossRef]